

# Functional assessment of morphological homoplasy in stem-gnathostomes

Humberto G. Ferrón,<sup>1,2,\*</sup>, Carlos Martínez-Pérez,<sup>1,2</sup>, Imran A. Rahman,<sup>3</sup>, Víctor Selles de Lucas,<sup>4</sup>, Héctor Botella,<sup>2</sup> and Philip C. J. Donoghue,<sup>1,\*</sup>

<sup>1</sup>School of Earth Sciences, University of Bristol, Life Sciences Building, Tyndall Avenue, Bristol BS8 1TQ, UK.

<sup>2</sup>Instituto Cavanilles de Biodiversidad i Biología Evolutiva, Universitat de València, C/ Catedrático José Beltrán Martínez, 2, 46980 Paterna, Valencia, Spain.

<sup>3</sup>Oxford University Museum of Natural History, Parks Road, Oxford OX1 3PW, UK.

<sup>4</sup>School of Engineering and Computer Science, University of Hull, Cottingham Rd, Hull HU6 7RX, UK.

\*Correspondence: [humberto.ferron@bristol.ac.uk](mailto:humberto.ferron@bristol.ac.uk), [phil.donoghue@bristol.ac.uk](mailto:phil.donoghue@bristol.ac.uk)

## ABSTRACT

Osteostraci and Galeaspida are stem gnathostomes, occupying a key phylogenetic position for resolving the nature of the jawless ancestor from which jawed vertebrates evolved more than 400 million years ago. Both groups are characterized by the presence of rigid headshields that share a number of common morphological traits, in some cases hindering the resolution of their interrelationships and the exact nature of their affinities with jawed vertebrates. Here, we explore the morphological and functional diversity of osteostracan and galeaspid headshields using geometric morphometrics and computational fluid dynamics to constrain the factors that promoted the evolution of their similar morphologies and informing on the ecological scenario under which jawed vertebrates emerged. Phylomorphospace, Mantel analysis and Stayton metrics demonstrate a high degree of homoplasy. Computational fluid dynamics reveals similar hydrodynamic performance among morphologically convergent species, indicating the independent acquisition of the same morphofunctional traits and, potentially, equivalent lifestyles. These results confirm that a number of the characters typically used to infer the evolutionary relationships among galeaspid, osteostracan and jawed vertebrates are convergent in nature, potentially obscuring understanding of the assembly of the gnathostome bodyplan. Ultimately, our results reveal that while the jawless relatives of the earliest jawed vertebrates were ecologically diverse, widespread convergence on the same hydrodynamic adaptations suggests they had reached the limits of their potential ecological diversity – overcome by jawed vertebrates and their later innovations.

## KEY WORDS

## 1. Introduction

The origin of jawed vertebrates (gnathostomes) was a key step in the evolutionary history of animals, culminating in the bodyplan shared by almost all living vertebrates [1]. This episode entailed more than simply the acquisition of jaws, also including a large and diverse suite of traits that distinguish living jawless and jawed vertebrates [2]. Fossil evidence demonstrates that the morphological gap between extant forms was once bridged by a disparate assemblage of extinct jawless (stem-gnathostome) vertebrate lineages, that record the sequential assembly of gnathostome characters [3,4]. Among these, Osteostraci and Galeaspida are of greatest significance because they represent the immediate jawless relatives of jawed vertebrates. While osteostracans are widely regarded as the sister-lineage of jawed vertebrates [5,6], their phylogenetic relationships are obscured by character reversal, convergence and missing data [2,7,8], and hence the competing clades Galeaspida+Osteostraci and Galeaspida+jawed vertebrates cannot be dismissed [8]. Indeed, the bodyplans of osteostracans and galeaspids exhibit gross similarity [9] (figure 1a), including bony headshields that have similar cephalic elaborations (elongated rostra, lateral expansions or processes) and vary between oblate and prolate cephalic profiles [10–13]. Ferrón *et al.* [14] showed that in osteostracans these structures represent adaptations for passive hydrodynamic control, including lift generation. Here, we attempt to provide insight into the ecology of the gnathostome ancestor by characterising quantitatively similarities in the anatomy of galeaspids and osteostracans and, through computational fluid dynamics (CFD), determine whether these similarities have a common functional basis. We found significant convergence in both the shape and hydrodynamic performance of both groups, compatible with the interpretation of their head shapes as adaptations to comparable lifestyles. We consider the implications and potential impact of these findings on current understanding of early vertebrate evolution and the ecological scenario preceding the emergence of jawed groups.

## 2. Materials and Methods

We characterized headshield morphological diversity in osteostracans and galeaspids in a phylogenetic context by means of geometric morphometrics to determine whether similarities in morphology reflect convergence or common descent. We then applied computational fluid dynamics to interrogate the resulting phylomorphospace (i.e. a projection of the phylogenetic tree into morphospace) from a functional perspective and evaluate if characteristics used in cladistic studies are compatible with convergent adaptations.

76

## 77 **(a) Geometric morphometrics**

78 Our study is limited to species of established taxa, with analyses performed at generic level,  
79 using one specimen per genus. We considered the type species and holotype specimen where  
80 possible; when this specimen was poorly preserved, another well-defined specimen or  
81 species was used instead. We incorporated a total of 59 specimens into the analysis, including  
82 30 osteostracans and 29 galeaspid, representing all major groups and the systematic breadth  
83 of both clades (electronic supplementary material, table S1).

84 We used geometric morphometrics to numerically describe the morphological diversity of  
85 osteostracan and galeaspid headshields following Ferrón *et al.* [14,15]. Landmark digitization  
86 was performed on photographic images of specimens from Ferrón *et al.* [15] and Zhu [12]  
87 using TpsDig v.2.26 [16] (electronic supplementary material, table S1). When one half of the  
88 headshield was poorly preserved or strongly deformed, the other half was mirrored; this  
89 approach has been shown to provide equivalent results to the analysis of complete unaltered  
90 structures at macroevolutionary scales [17]. When preservation issues and/or deformation  
91 were minor, no corrections were implemented in order to avoid the introduction of additional  
92 human error and given that biological signal is still maintained in those cases [18]. Our  
93 landmark configuration included a total of 6 landmarks of type I and II, and 82 landmarks of  
94 type III that were equally interpolated along the specimen outline in four different open  
95 curves (figure 1b). Generalized Procrustes analysis (GPA) was performed in MorphoJ v. 1.06d  
96 [19] to remove the variation in translation, rotation and size from the original landmark  
97 configurations. No sliding methods for Type III landmarks were implemented. We obtained  
98 Euclidean distance matrices which were subjected to principal coordinate analysis in R [20]  
99 using the packages ‘cluster’ [21] and ‘ape’ [22].

100

## 101 **(b) Morphological homoplasy analyses**

102 The relationship between morphospace occupation and phylogeny were explored by  
103 constructing and visualizing phylomorphospaces. These were generated using the R packages  
104 ‘Phytools’ [23] and ‘ggplot2’ [24] based on pre-ordination ancestral state reconstruction [25]  
105 through stochastic character state mapping [26] in the R package ‘geomorph’ [27]. Our tree  
106 is based on the phylogenetic hypotheses and stratigraphic ranges published by Zhu *et al.* [11],  
107 Gai *et al.* [13,28], Sansom [10], and Sansom *et al.* [29], after modification in Mesquite [30]  
108 and time-calibration in the R package ‘paleotree’ [31].

109

110 Morphological homoplasy was quantified following two different procedures. First, we  
111 determined the strength and significance of linear correlations among the distance matrices  
112 derived from morphometric and phylogenetic data (i.e., phenetic vs phylogenetic distances)  
113 by implementing Mantel tests considering the whole dataset, only osteostracans, and only  
114 galeaspid in the R package ‘vegan’ [32]. Distance matrices show greater decoupling and,  
115 consequently, lower correlation where homoplasy occurs. Secondly, we considered the C1

metric of Stayton [33], which quantifies the ratio of the phenotypic distance between putatively convergent taxa ( $D_{tip}$ ) and the maximum phenotypic distance between any pair of ancestors ( $D_{max}$ ) as:

$$C1 = 1 - (D_{tip} / D_{max})$$

C1 ranges from 0 to 1, where 1 indicates complete convergence. C1 was calculated for different osteostracan-galeaspid pairs, selecting representatives of all major clades of both groups. To test significance of the measured C1 values, we ran 1000 simulations for each pair using Brownian Motion models in order to determine if the observed C1 value is greater than expected by chance. These analyses were conducted in the R package ‘convevol’ [34].

### (c) Three-dimensional virtual modelling

We created three dimensional digital models for eight species of osteostracans (*Boreaspis ceratops*, *Cephalaspis lyelli*, *Hemicyclaspis murchisoni*, *Hoelaspis angulata*, *Kiaeraspis auchenaspidoides*, *Spatulaspis robusta*, *Stensiopelta pustulata* and *Tremataspis schmidtii*) and five species of galeaspid (*Geraspis rara*, *Macrothyraspis longicornis*, *Pentathyraspis pelta*, *Polybranchiaspis liaojiaoshanensis* and *Rhegmaspis xiphoidea*), which constitute a good representation of all occupied areas of the phylomorphospace. Digital models were built in 3D Studio Max based on published reconstructions in several views and/or photographs of fossil specimens (electronic supplementary material, table S2). For most of the selected species, well-preserved fossil headshields are known, ensuring these parts could be modelled accurately. The postcranial region was modelled for species in which it is known (i.e., *C. lyelli* [35], *H. murchisoni* [36], *T. schmidtii* [37] and *G. rara* [12]), whereas a generalized osteostracan or galeaspid morphology based on existing published reconstructions was considered for the remaining taxa. The resulting three-dimensional models were scaled to life size using Netfabb Basic and converted into NURBS surfaces in Geomagic Studio ([www.geomagic.com](http://www.geomagic.com)). Osteostracan models correspond to those used in Ferrón *et al.* [14].

### (d) Computational fluid dynamics analyses

Computational fluid dynamics is a computational method for simulating fluid flow (liquids or gases) and their interaction with solid surfaces, enabling large-scale comparative analyses for resolving functional and ecological hypotheses in extinct taxa [38]. We performed simulations of water flow around the three-dimensional models in COMSOL Multiphysics 5.2 (<http://www.comsol.com>), following the procedure outlined in Ferrón *et al.* [14]. Pelagic and benthic conditions were emulated in order to assess the functional constraints of homoplasy in different ecological scenarios. For the pelagic scenario, the computational domain consisted of a cylinder (1500 mm in length and 300 mm in diameter), with the three-dimensional model centrally located and positioned at eight different angles of attack (from 0° to 70°, every 10°) (figure 1c). For the benthic scenario, the computational domain consisted of a half-cylinder (1500 mm in length and 300 mm in diameter), with the three-

dimensional model positioned at 0.1, 0.5 and 1.0 body lengths above the lower surface of the domain (figure 1c).

An inlet with a normal inflow velocity boundary condition, with a turbulence intensity of 0.05, was specified at the anterior end of the domain; and an outlet with a zero pressure boundary condition was defined at the opposing end. Boundaries at the water–fossil interface were ‘solid’ (i.e., no-slip boundary condition) whereas the boundaries at the top and sides of the domain were ‘open’ (i.e., slip boundary condition). In the benthic scenario, a moving wall boundary condition with the same velocity as the inlet was assigned to the flat lower boundary of the half-cylinder. The domain was meshed in COMSOL Multiphysics using free tetrahedral elements and the ‘normal’ mesh size parameter. Previous work has demonstrated that CFD results are independent of the domain and mesh sizes under this experimental setting within the range of body sizes considered in our analysis [14].

We simulated three-dimensional incompressible flow through the domain, using a stationary solver to compute the steady-state flow patterns, considering a flow velocity of  $0.30 \text{ m s}^{-1}$  (Reynolds numbers of 17100 to 64500). This constitutes a realistic swimming velocity according to records of similar sized living fishes [39]. The shear stress transport (SST) turbulence model and a segregated solver algorithm were used to solve the Reynolds averaged Navier-Stokes (RANS) equations. The choice of the RANS SST model is based on its reduced computational requirements and potential for capturing the same general flow patterns than other more refined models (e.g., large eddy simulation) [40]. Segregated iterations terminated when the relative error was lower than the relative tolerance (0.001). We carried out additional simulations with inlet velocities of  $0.65$  and  $1.00 \text{ m s}^{-1}$  (Reynolds numbers of 37050 to 215000) in order to test the effect of increasing inlet velocity (electronic supplementary material, table S3).

Flow patterns over the surface of the three-dimensional models were visualized using plots of vorticity (Z-vorticity,  $\text{s}^{-1}$ ) and pressure (Pa). Drag and lift forces ( $C_D$  and  $C_L$ ) acting on the surfaces of the models were calculated using the headshield area as the reference area (electronic supplementary material, table S2). Heat maps of the  $C_D$  and  $C_L$  were constructed and plotted over the phylomorphospaces using the R package “akima” [41]. Correlation between headshield morphology and hydrodynamic parameters (i.e.,  $C_D$  and  $C_L$ ) was assessed through phylogenetic generalized least square (PGLS) analysis in MorphoJ v. 1.06d [19]. PGLS were undertaken for three pelagic (at  $0^\circ$ ,  $10^\circ$  and  $20^\circ$ ) and one benthic ( $0.1_{BL}$ ) simulations, which were considered the most biologically realistic scenarios as evidenced by living fishes [42]. In order to evaluate the biological relevance of the calculated forces, the apparent weight of each taxon was inferred from the model volume, assuming a body density of  $1100 \text{ kg m}^{-3}$  [43]. This value represents a reasonable estimate for osteostracans and galeaspid in light of the body densities calculated for other jawless stem-gnathostomes where the

distribution and density of dermal bone, soft tissues and internal cavities is taken into account [44].

### 3. Results

#### (a) Geometric morphometrics and homoplasy tests

Osteostracans and galeaspids occupy similar regions of the morphospace, with most of their representatives located in positive scores on PCo1 and PCo3 (figure 2a). Only a few regions are exclusively occupied either by osteostracans or galeaspids: osteostracans with comparatively narrow headshields and poorly developed cornual processes occupy the region of morphospace that is strongly negative on PCo1 and strongly positive on PCo2; and long-snouted galeaspids with long and thin lateral cephalic processes occupy the region of morphospace that is strongly positive on PCo1 and strongly negative on PCo2 and PCo3. The phylomorphospace exhibits a large number of intersections among galeaspid and osteostracan clades and, at least, two strong branching trends (figure 2a). The trends in osteostracans occur along PCo1 and PCo3, one characterized by the reduction and eventual loss of the cornuae, and the other correlating with the acquisition of well-developed cornual processes and elongated rostra. The trends in galeaspids are captured along PCo1–3, one characterized by the elongation of the rostrum, and another correlating with the acquisition of both expanded lateral processes and long rostra (figure 2a). The results of the Mantel tests indicate significant correlation between phenetic and phylogenetic distances in both the total dataset and the galeaspid subset ( $p$ -value = 0.003 in both cases), but not in the osteostracan subset ( $p$ -value = 0.653). Mantel  $r$  statistic ranged between -0.030 and 0.313 in all analyses (figure 2b). Stayton metrics analyses reveal that 42 of the 169 tested pairs of osteostracans-galeaspids show C1 values significantly greater than those expected under Brownian motion evolution (figure 2b and electronic supplementary material, table S4).

#### (b) Computational fluid dynamics

For all tested species, the highest drag coefficients ( $C_D$ ) occur at higher angles of attack and in closer proximity to the substrate (electronic supplementary material, figure S1 and table S3). In the pelagic scenario, the lift coefficient ( $C_L$ ) increases linearly with angle of attack, reaching a maximum at 40°–50° before attaining the stall angle of attack, from which  $C_L$  decreases abruptly (electronic supplementary material, figure S1 and table S3). Usually, absolute lift force overcomes apparent weight at realistic swimming speeds and angles of attack (between 10° and 40°) in all taxa (electronic supplementary material, table S3). Under benthic conditions,  $C_L$  increases considerably for all models when they are placed in proximity to the substrate (electronic supplementary material, figure S1 and table S3), but this phenomenon is more evident in some species with dorso-ventrally oblate headshields such as for example the osteostracans *Stensiopelta* and *Boreaspis*, or the galeaspids *Geraspis*, *Pentathyraspis* and *Polybranchiaspis*. The extra lift force generated when the models are located at 0.1 body lengths above the substrate is enough to counteract the apparent body weight of most of the

taxa (electronic supplementary material, table S3). The lift to drag ratio (L/D), considered a measure of hydrodynamic efficiency, shows important variations among the different species and tested experimental conditions (electronic supplementary material, figure S1 and table S3). In the pelagic scenario, most of the species attain maximum L/D at angles of attack between 20° and 30° (except for the osteostracan *Hoelaspis*, where it is reached at 40°). Under benthic conditions, all species attain the highest L/D when they are placed at 0.1 body lengths above the substrate. In general terms, species with dorso-ventrally prolate headshields reach the maximum L/D under pelagic conditions whereas species with dorso-ventrally oblate headshields show the peak L/D under benthic scenarios. Generally, convergent species pairs (supported by Stayton metrics) exhibit maximum L/D in the same ecological scenario, but there are exceptions to this rule (*Boreaspis* vs *Macrothyraspis*; *Hemicyclaspis*, vs *Geraspis*, *Pentathyraspis*, and *Polybranchiaspis*).

$C_D$  and  $C_L$  heat maps plotted over phylomorphospaces reveal very similar patterns when considering osteostracans and galeaspids separately under pelagic scenarios at 0° angle of attack (figure 3a). In both cases, the highest  $C_D$  values are associated with positive scores on PCo1–3 and the highest  $C_L$  values correlate with negative and positive scores of PCo1 and PCo2, respectively. Similar patterns in the  $C_D$  and  $C_L$  heat maps derived from osteostracans and galeaspids are also evident in other tested scenarios (electronic supplementary material, data S1). Morphological aspects correlated with the generation of drag and lift show important similarities in both osteostracans and galeaspids (figure 3b). Thus,  $C_D$  is significantly correlated in both groups with the degree of development of headshield lateral expansions in benthic and pelagic scenarios at angles of attack ranging 0–20°. On the other hand,  $C_L$  correlates with headshield morphology in pelagic scenarios at low angles of attack (i.e., from 0–10° in osteostracans, and 0° in galeaspids) where species with delta-shaped headshields show the highest  $C_L$  values. Otherwise, no significant correlation is detected between  $C_L$  and headshield morphology in benthic scenarios.

The distribution of tip vortices is similar within convergent pairs of osteostracans and galeaspids (figure 4). In species whose headshields exhibit well-developed lateral processes, tip vortices form in more distal positions separated from the body, whereas in species lacking prominent lateral processes, the tip vortices remain close or attached to the body surface. In general, the intensity of these vortices is similar in convergent taxa, excepting the *Boreaspis* vs *Macrothyraspis* pairing, where they are less developed in *Macrothyraspis*. The patterns of pressure over the headshields show significant differences between the pelagic and benthic scenarios (electronic supplementary material, figure S2). In the pelagic simulations, the highest pressures occur on the snout, whereas in the benthic simulations they expand along most of the ventral surface, especially in species with dorso-ventrally oblate headshields (e.g., *Stensiopelta*, *Boreaspis*, *Geraspis*, and *Pentathyraspis*).

#### 4. Discussion

## **(a) Similar galeaspid and osteostracan headshields result from widespread convergence**

Our results reveal widespread convergence in the morphology of the headshields of osteostracans and galeaspids, supported both by qualitative interpretation of phylomorphospaces and quantitative metrics (figure 2). Despite significant correlation between phenetic and phylogenetic distances, the Mantel  $r$  statistic is comparatively low in all analyses, indicating that correlations are weak and suggesting widespread morphological convergence (figure 2b). Stayton metric analyses provide further support, indicating that a large number of osteostracans and galeaspids, including representatives of several major groups of both lineages, evolved to be more similar to each other than would be expected under a null evolutionary model of Brownian motion (figure 2b and electronic supplementary material, table S4). The most remarkable instances of convergence include forms with elongate rostra (e.g., *Spatulaspis* vs *Rhegmaspis*), expanded lateral processes (*Cephalaspis*, *Tegaspis*, *Stensiopelta*, and *Auchenaspis* vs *Eugaleaspis*, *Geraspis*, and *Zhaotongaspis*), both elongated rostra and expanded lateral processes (e.g., *Boreaspis* vs *Pterogonaspis*, *Sanchaspis*, and *Macrothyraspis*), and more fusiform headshields (*Hemicyclaspis*, and *Kiaeraspis* vs *Pentathyraspis*, *Lopadaspis*, and *Polybranchiaspis*); in many cases, these pairs exhibit  $p$ -values  $< 0.01$ .

## **(b) Convergence generally correlates with hydrodynamic performance**

Exploration of the hydrodynamic properties of the morphospace circumscribed by osteostracan and galeaspid headshields revealed that morphological convergence correlates with morphofunctional traits and, potentially, equivalent lifestyles and ecologies. Discrete regions of the morphospace are occupied by osteostracans and galeaspids that show comparable hydrodynamic performance (figure 3a and electronic supplementary material, data S1). In fact, we detected significant correlations between hydrodynamic forces (i.e.,  $C_D$  and  $C_L$ ) and equivalent headshield structures in both groups (figure 3b). Morphologically comparable osteostracan and galeaspid headshields exhibit remarkably similar patterns of hydrodynamic flow, as revealed by vorticity and pressure visualizations (figure 4 and electronic supplementary material, figure S2). The distribution and intensity of tip vortices is similar in most of the convergent species pairs (figure 4). These vortices originate at the tips of cornual or inner cornual processes, similar to aircraft wingtips [45]. In general terms, species with high aspect ratios (e.g., *Boreaspis* and *Machairaspis*) exhibit less intense tip vortices because of less important tip losses (i.e., fluid leakage between the lower and upper surfaces), which generate smaller induced drag. However, high aspect ratios result in lower manoeuvrability due to a larger moment of inertia [45]. Similar vorticity patterns have been reported previously in other groups of stem-gnathostomes [46]. Likewise, the distribution of pressure around the models suggest some common biomechanical properties in osteostracan and galeaspids with similar shaped headshields (electronic supplementary material, figure S2). Thus, headshields that are oblate in cross-section exhibit a greater increase in pressure on the ventral surface and considerably higher lift generation when they are placed close to the substrate (electronic supplementary material, figures S1 and S2 and table S3). This is



indicative of ground effect, a phenomenon that many living benthic species benefit from, which entails modification of fluid flow below the body, increasing lift and facilitating enhanced hydrodynamic efficiency when moving close to the substrate [47].

Among the convergent groupings of osteostracans and galeapids, only *Boreaspis* and *Macrothyraspis*, characterized by long rostra and lateral expansions in the headshields, exhibit significant differences in hydrodynamic performance. When compared to *Boreaspis*, *Macrothyraspis* exhibits much more poorly-developed vortices (figure 4) and a less intense ground effect (electronic supplementary material, figures S1 and S2), both of which result in very distinct trends in  $C_D$  and  $C_L$  in most of the tested scenarios (electronic supplementary material, figure S1 and table S3). Thus, this particular instance of convergence cannot be correlated with hydrodynamic performance; rather, the acquisition of long rostra and lateral expansions must have been driven by other factors, including predator deterrence [48], housing sense organs [49], substrate anchoring [50], or specialised feeding strategies [51].

### **(c) Implications for phylogenetic analyses of early vertebrate evolution**

Our study identifies a number of convergent traits in the headshields of galeaspids and osteostracans. This is of concern since the headshield comprises the character complex from which the vast majority of phylogenetic characters are derived [15] and competing hypotheses on the phylogenetic relationships of galeaspids, osteostracans and jawed vertebrates are discriminated by few characters [5,52]. Characteristics including the cross-sectional (oblate versus prolate) and dorso-ventral profiles of the headshield, presence or absence of cornual/corner processes, rostral processes, serrate versus entire margin of the headshield, have all been used to resolve the phylogeny of galeaspids and osteostracans [6,10,11,52–54] and yet they are clearly convergent, correlating with hydrodynamic properties. Furthermore, while we have considered only galeaspids and osteostracans, other stem-gnathostome clades, including thelodonts [55,56] and pteraspidomorphs [57,58], exhibit anatomical features compatible with hydrodynamic adaptation. The exclusion of these characters, together with inclusion of recently identified similarities between galeaspids and jawed vertebrates [7,8], is likely to lead to a shake-up of received wisdom concerning the relationships among stem-gnathostomes, changing perceptions of character evolution in the assembly of the gnathostome bodyplan.

### **(d) Implications for the ecological scenario preceding the emergence of jawed vertebrates**

Our results provide additional support for the view that the immediate jawless relatives of the earliest jawed vertebrates were already ecologically diverse [14], showing a range of adaptations for passively controlling flow around the body. These adaptations could have provided stem-gnathostomes with higher manoeuvrability and versatility for adopting a greater diversity of locomotory strategies than previously thought (conventional interpretations view stem-gnathostomes as benthic mud-grubbers with poor swimming capabilities [59–62]). Among these convergent adaptations, cornual processes have

sometimes been considered as structures to protect the pectoral fins in osteostracans [63]. However, given the lack of paired appendages in galeaspid, we propose that cornual processes represent independent adaptations to generating lift, later enhanced by the acquisition of pectoral fins in osteostracans, and eventually rendered redundant by the more flexible and muscular fins of jawed vertebrates. The high degree of morphological homoplasy among galeaspid and osteostracans, with the evolution of largely the same set of hydrodynamic adaptations in both groups, might imply that they had approached the limits of ecological diversity that could be achieved by the bodyplan of jawless vertebrates [64]. The evolution of jawed vertebrates built upon the bodyplan and anatomical constraints that galeaspid and osteostracans manifest. Key innovations including paired pelvic fins, a mineralised vertebral skeleton, and a pectoral girdle distinct from the head and jaws, all served to release these constraints, allowing jawed vertebrates to assume greater ecological diversity and, thus, dominance over their jawless kin [65–67].

## 5. Conclusions

The headshields of osteostracans and galeaspid show a high degree of morphological homoplasy, as suggested by geometric morphometrics, phylomorphospace analysis and different quantitative metrics of convergence. Computational fluid dynamics analyses reveal that most of the detected convergent traits are compatible with morphofunctional adaptations, thus suggesting that the acquisition of similar morphologies in both groups may relate to the evolution of similar lifestyles. The exclusion of these characters in future phylogenetic analyses, and the consideration of recently identified similarities between galeaspid and jawed vertebrates, may change our current perception on the relationships among stem-gnathostomes and on the evolution of the gnathostome bodyplan. Ultimately, this finding further supports ecological diversification among the immediate jawless relatives of all jawed vertebrates and the prevalence of adaptations for passively controlling the flow around the body in these groups, which may have conferred them greater manoeuvrability and locomotory capabilities than previously thought.

## Data accessibility

Data and R code are available from the Dryad Digital Repository: <https://doi.org/10.5061/dryad.9s4mw6mfd>.

## FUNDING

This work was supported by the European Commission [grant number H2020-MSCA-IF-2018-839636]; and the Oxford University Museum of Natural History.

## ACKNOWLEDGEMENTS

We thank two anonymous reviewers for providing thoughtful and valuable comments on the manuscript.

## REFERENCES

1. Brazeau MD, Friedman M. 2015 The origin and early phylogenetic history of jawed vertebrates. *Nature* **520**, 490–497. (doi: 10.1038/nature14438)
2. Brazeau MD, Friedman M. 2014 The characters of Palaeozoic jawed vertebrates. *Zool. J. Linnean Soc.* **170**, 779–821. (doi: 10.1111/zoj.12111)
3. Janvier P. 2001 Ostracoderms and the shaping of the gnathostome characters. In *Major Events in Early Vertebrate Evolution* (ed. PE Ahlberg), pp. 172–186. New York, US: Taylor and Francis.
4. Donoghue PCJ, Keating JN. 2014 Early vertebrate evolution. *Palaeontology* **57**, 879–893. (doi: 10.1111/pala.12125)
5. Janvier P. 1984 The relationships of the Osteostraci and Galeaspida. *J. Vertebr. Paleontol.* **4**, 344–358. (doi: 10.1080/02724634.1984.10012014)
6. Janvier P. 1996 *Early vertebrates*. Oxford, UK: Clarendon Press.
7. Gai Z, Donoghue PC, Zhu M, Janvier P, Stampanoni M. 2011 Fossil jawless fish from China foreshadows early jawed vertebrate anatomy. *Nature* **476**, 324–327. (doi: 10.1038/nature10276)
8. Gai Z-K, Zhu M, Donoghue PC. 2019 The circulatory system of Galeaspida (Vertebrata; stem-Gnathostomata) revealed by synchrotron X-ray tomographic microscopy. *Palaeoworld* **28**, 441–460. (doi: 10.1016/j.palwor.2019.04.005)
9. Janvier P. 1993 Patterns of diversity in the skull of jawless fishes. In *The skull* (eds. J Hanken, BK Hall), pp. 131–188. Chicago, US: Chicado University Press.
10. Sansom RS. 2009 Phylogeny, classification and character polarity of the Osteostraci (Vertebrata). *J. Syst. Palaeontol.* **7**, 95–115. (doi: 10.1017/S1477201908002551)
11. Zhu M, Gai Z. 2007 Phylogenetic relationships of galeaspids (Agnatha). *Front. Biol. China* **2**, 151–169. (doi: 10.1007/s11515-007-0022-6)
12. Zhu M. 2015 *Palaeovertebrata Sinica: Fishes. Agnathans*. Beijing, China: Science Press.
13. Gai ZK, Zhu M, Jia LT, Zhao WJ. 2015 A streamlined jawless fish (Galeapida) from the Lower Devonian of Yunnan, China and its taxonomic and paleoecological implications. *Vertebrat. Palasiatic.* **53**, 93–109.
14. Ferrón HG, Martínez-Pérez C, Rahman IA, Selles de Lucas V, Botella H, Donoghue PCJ. 2020 Computational fluid dynamics suggests ecological diversification among stem-gnathostomes. *Curr. Biol.* **30**, 1–6. (doi: 10.1016/j.cub.2020.09.031)
15. Ferrón HG, Greenwood JM, Deline B, Martínez-Pérez C, Botella H, Sansom RS, Ruta M, Donoghue PCJ. 2020 Categorical versus geometric morphometric approaches to characterizing the evolution of morphological disparity in Osteostraci (Vertebrata, stem Gnathostomata). *Palaeontology* **63**, 717–732. (doi: 10.1111/pala.12482)
16. Rohlf J. 2016 tpsDig2. v 2.26. *Stony Brook University, New York* **523**.

- 434 17. Cardini A. 2016 Lost in the other half: improving accuracy in geometric morphometric analyses of  
 435 one side of bilaterally symmetric structures. *Syst. Biol.* **65**, 1096–1106. (doi:  
 436 10.1093/sysbio/syw043)
- 437 18. Angielczyk KD, Sheets HD. 2007 Investigation of simulated tectonic deformation in fossils using  
 438 geometric morphometrics. *Paleobiology* **33**, 125–148. (doi: 10.1666/06007.1)
- 439 19. Klingenberg CP. 2011 MorphoJ: an integrated software package for geometric morphometrics.  
 440 *Mol. Ecol. Resour.* **11**, 353–357. (doi: 10.1111/j.1755-0998.2010.02924.x)
- 441 20. R Development Core Team. 2020 *R: A language and environment for statistical computing*. R  
 442 Foundation for Statistical Computing, Vienna.
- 443 21. Maechler M, Rousseeuw P, Struyf A, Hubert M, Hornik K. 2019 *cluster: Cluster Analysis Basics and*  
 444 *Extensions*. R package version 2.1.0.
- 445 22. Paradis E, Schliep K. 2018 ape 5.0: an environment for modern phylogenetics and evolutionary  
 446 analyses in R. *Bioinformatics* **35**, 526–528. (doi: 10.1093/bioinformatics/bty633)
- 447 23. Revell LJ. 2012 phytools: an R package for phylogenetic comparative biology (and other things).  
 448 *Methods Ecol. Evol.* **3**, 217–223. (doi: 10.1111/j.2041-210X.2011.00169.x)
- 449 24. Wickham H. 2016 *ggplot2: elegant graphics for data analysis*. Houston, US: Springer. (doi:  
 450 10.1007/978-3-319-24277-4)
- 451 25. Lloyd GT. 2018 Journeys through discrete-character morphospace: synthesizing phylogeny,  
 452 tempo, and disparity. *Palaeontology* **61**, 637–645. (doi: 10.1111/pala.12380)
- 453 26. Huelsenbeck JP, Nielsen R, Bollback JP. 2003 Stochastic mapping of morphological characters.  
 454 *Syst. Biol.* **52**, 131–158. (doi: 10.1080/10635150390192780)
- 455 27. Adams DC, Collyer M, Kaliontzopoulou A, Sherratt E. 2019 *Geomorph: Software for geometric*  
 456 *morphometric analyses*. R package version 3.1.0.
- 457 28. Gai Z, Lu L, Zhao W, Zhu M. 2018 New polybranchiaspiform fishes (Agnatha: Galeaspida) from the  
 458 Middle Palaeozoic of China and their ecomorphological implications. *PLoS ONE* **13**, e0202217. (doi:  
 459 10.1371/journal.pone.0202217)
- 460 29. Sansom RS, Randle E, Donoghue PCJ. 2015 Discriminating signal from noise in the fossil record of  
 461 early vertebrates reveals cryptic evolutionary history. *Proc. Royal Soc. B.* **282**, 20142245. (doi:  
 462 10.1098/rspb.2014.2245)
- 463 30. Maddison WP, Maddison DR. 2019 *Mesquite: a modular system for evolutionary analysis*. Version  
 464 3.51. 2018.
- 465 31. Bapst DW. 2012 paleotree: an R package for paleontological and phylogenetic analyses of  
 466 evolution. *Methods Ecol. Evol.* **3**, 803–807. (doi: 10.1111/j.2041-210X.2012.00223.x)
- 467 32. Oksanen J *et al.* 2013 Package ‘vegan’. *Community ecology package*, version 2.
- 468 33. Stayton CT. 2015 The definition, recognition, and interpretation of convergent evolution, and two  
 469 new measures for quantifying and assessing the significance of convergence. *Evolution* **69**, 2140–  
 470 2153. (doi: 10.1111/evo.12729)

- 471 34. Stayton CT. 2017 *Convevol: Analysis of convergent evolution. R package version 1.*
- 472 35. White EI. 1958 On *Cephalaspis lyelli* Agassiz. *Palaeontology* **1**, 99–105.
- 473 36. Stensio EA. 1932 *The Cephalaspids of Great Britain*. London, UK: British Museum Natural History.
- 474 37. Janvier P. 1985 Les Thyestidiens (Osteostraci) du Silurien de Saaremaa (Estonie). Première partie:  
475 Morphologie et anatomie. *Ann. de Paleontol.* **71**, 83–147.
- 476 38. Rahman IA. 2017 Computational fluid dynamics as a tool for testing functional and ecological  
477 hypotheses in fossil taxa. *Palaeontology* **60**, 451–459. (doi: 10.1111/pala.12295)
- 478 39. Videler JJ. 1993 *Fish swimming*. London, U.K.: Chapman & Hall. (doi: 10.1007/978-94-011-1580-3)
- 479 40. Gibson BM, Furbish DJ, Rahman IA, Schmeeckle MW, Laflamme M, Darroch SA. 2020 Ancient life  
480 and moving fluids. *Biol. Rev.* (in press). (doi: 10.1111/brv.12649)
- 481 41. Akima H, Gebhardt A, Petzold T, Maechler M. 2016 *Package 'akima'*.
- 482 42. He P, Wardle n C. 1986 Tilting behaviour of the Atlantic mackerel, *Scomber scombrus*, at low  
483 swimming speeds. *J. Fish Biol.* **29**, 223–232. (doi: 10.1111/j.1095-8649.1986.tb05013.x)
- 484 43. Lowndes AG. 1955 XXXII.—Density of fishes: Some notes on the swimming of fish to be correlated  
485 with density, sinking factor and load carried. *Ann. Mag. Nat. Hist.* **8**, 241–256. (doi:  
486 10.1080/00222935508655637)
- 487 44. Botella H. 2005 Microictiolitos del devónico inferior de nigüella (cordillera ibérica);  
488 consideraciones paleobiológicas e hidrodinámicas de condriactos y agnatos primitivos.  
489 (Universitat de València.
- 490 45. Çengel YA, Cimbala V. 2018 *Fluid mechanics: fundamentals and applications*. New York, US:  
491 McGraw-Hill Education.
- 492 46. Dec M. 2019 Hydrodynamic performance of psammosteids: New insights from computational  
493 fluid dynamics simulations. *Acta Palaeontol. Pol.* **64**, 679–684. (doi: 10.4202/app.00623.2019)
- 494 47. Vogel S. 1994 *Life in moving fluids: the physical biology of flow*. New Jersey, US: Princeton  
495 University Press.
- 496 48. Janvier P. 1997 Contribution à la connaissance de l'anatomie et de la systématique du genre  
497 *Boreaspis* Stensiö (Agnatha, Cephalaspidomorphi, Osteostraci), du Dévonien inférieur du  
498 Spitsberg. *Ann. de Paleontol., Vertébrés* **63**, 1–32.
- 499 49. Voichyshyn V. 2006 New osteostracans from the Lower Devonian terrigenous deposits of Podolia,  
500 Ukraine. *Acta Palaeontol. Pol.* **51**, 131–142.
- 501 50. Janvier P. 1985 *Les Céphalaspides du Spitsberg. Anatomie, phylogénie et systématique des*  
502 *Ostéostracés siluro-dévonien. Révision des Ostéostracés de la formation de Wood Bay (Dévonien*  
503 *inférieur du Spitsberg)*. Paris, France: CNRS édition.
- 504 51. Dineley DL. 1994 Cephalaspids from the Lower Devonian of Prince of Wales Island, Canada.  
505 *Palaeontology* **37**, 61–70.

- 506 52. Donoghue PCJ, Forey PL, Aldridge RJ. 2000 Conodont affinity and chordate phylogeny. *Biol. Rev.*  
507 **75**, 191–251. (doi: 10.1017/s0006323199005472)
- 508 53. Sansom RS. 2008 The origin and early evolution of the Osteostraci (Vertebrata): a phylogeny for  
509 the Thyestiida. *J. Syst. Palaeontol.* **6**, 317–332. (doi: 10.1017/S1477201907002386)
- 510 54. Miyashita T *et al.* 2019 Hagfish from the Cretaceous Tethys Sea and a reconciliation of the  
511 morphological–molecular conflict in early vertebrate phylogeny. *PNAS* **116**, 2146–2151. (doi:  
512 doi.org/10.1073/pnas.1814794116)
- 513 55. Fletcher TM. 2015 The Evolution of Speed: an empirical and comparative analysis of drag-reducing  
514 scales in early fishes. University of Leeds.
- 515 56. Ferrón HG, Botella H. 2017 Squamation and ecology of thelodonts. *PLoS ONE* **12**, e0172781. (doi:  
516 doi.org/10.1371/journal.pone.0172781)
- 517 57. Botella H, Fariña RA. 2008 Flow pattern around the rigid cephalic shield of the Devonian agnathan  
518 *Errivaspis waynensis* (Pteraspidoformes: Heterostraci). *Palaeontology* **51**, 1141–1150. (doi:  
519 10.1111/j.1475-4983.2008.00801.x)
- 520 58. Davies BE. 2009 An experimental morphological investigation into the hydrodynamics and  
521 locomotion of the Palaeozoic jawless vertebrates *Poraspis*, *Errivaspis* and *Ateleaspis*. University  
522 of Leicester.
- 523 59. Aleyev Y, Novitskaya LI. 1983 Experimental study of hydrodynamic qualities of Devonian  
524 heterostracans. *Paleontol. J.* **1**, 3–12.
- 525 60. White EI, Toombs HA. 1983 The cephalaspids from the Dittonian section at Cwm Mill, near  
526 Abergavenny, Gwent. *Bull. br. Mus. nat. Hist. Geol.* **37**, 149–171.
- 527 61. Belles-Isles M. 1987 La nage et l'hydrodynamique de deux Agnathes du Paléozoïque: *Alaspis*  
528 *macrotuberculata* et *Pteraspis rostrata*. *Neues Jahrb. Geol. Palaeontol. Abh.* **175**, 347–376.
- 529 62. Mark-Kurik E. 1992 Functional aspects of the armour in the early vertebrates. In *Fossil fishes as*  
530 *living animals* (ed. E Mark-Kurik), pp. 107–115. Tallin, Estonia: Academy of Sciences of Estonia.
- 531 63. Carlsson A. 2006 Description of a new osteostracan species from Ukraine with a brief analysis of  
532 the interrelationships of Scolenaspida. Uppsala University.
- 533 64. Oyston JW, Hughes M, Wagner PJ, Gerber S, Wills MA. 2015 What limits the morphological  
534 disparity of clades? *Interface focus* **5**, 20150042. (doi: 10.1098/rsfs.2015.0042)
- 535 65. Anderson PS. 2008 Shape variation between arthrodire morphotypes indicates possible feeding  
536 niches. *J. Vertebr. Paleontol.* **28**, 961–969. (doi: 10.1671/0272-4634-28.4.961)
- 537 66. Anderson PS, Friedman M, Brazeau MD, Rayfield EJ. 2011 Initial radiation of jaws demonstrated  
538 stability despite faunal and environmental change. *Nature* **476**, 206. (doi: 10.1038/nature10207)
- 539 67. Hill JJ, Puttick MN, Stubbs TL, Rayfield EJ, Donoghue PC. 2018 Evolution of jaw disparity in fishes.  
540 *Palaeontology* **61**, 847–854. (doi: 10.1111/pala.12371)



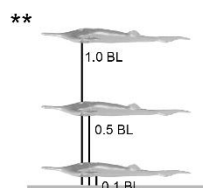
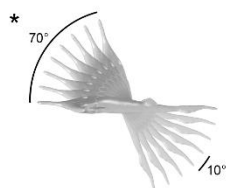
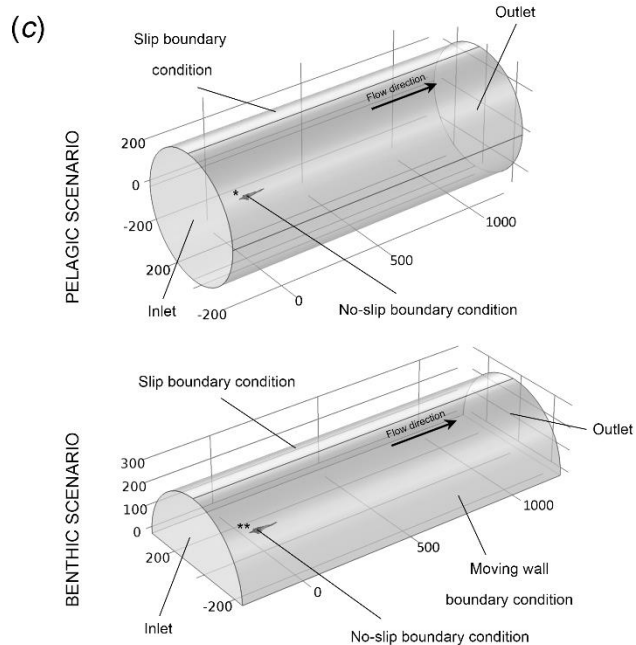
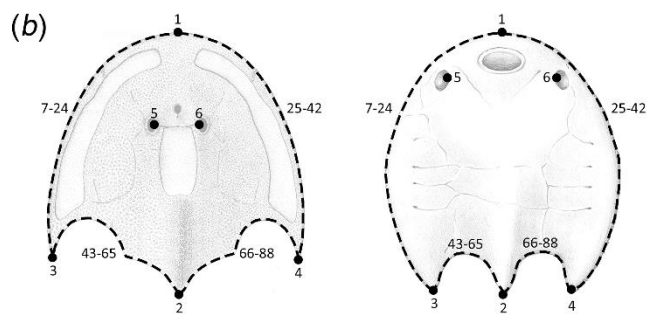
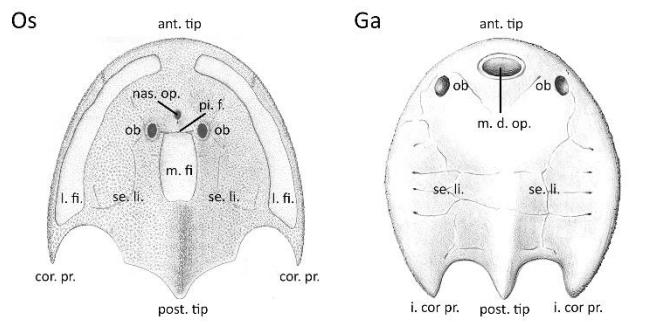
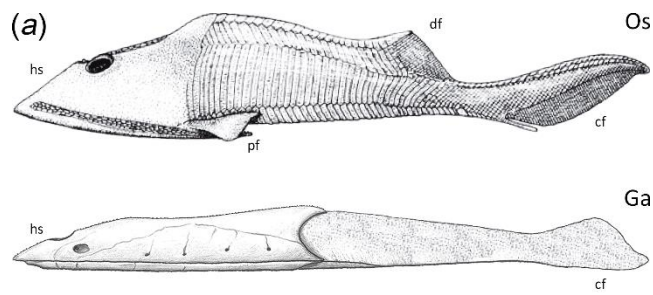




**Figure 1.** General morphology of osteostracans and galeaspids and experimental setup used in computational fluid dynamics simulations. (a) Anatomy of the body and headshield of a well-known osteostracan (Os) and galeaspid (Ga), showing the location of the pectoral fins (pf), dorsal fin (df), caudal fin (cf), headshield (hs), anterior and posterior tips of the headshield (ant. tip. and post. tip, respectively), cornual processes (cor. pr.), inner cornual processes (i. cor. pr.), sensory lines (se. li.), eye orbits (ob.), nasohypophysial opening (nas. op.), pineal foramen (pi. f.), median and lateral fields (m. fi. and l. fi. respectively), and median dorsal opening (m. d. op.). Osteostracan whole body and galeaspid drawings modified from Janvier [6]: figs. 4.14A1, 4.19A1 and 4.19A2. Osteostracan headshield drawing modified from Janvier [50]: fig. 99. (b) Landmark configuration used in the geometric morphometric analysis. Landmark 1, anterior tip of the headshield or the rostral process. Landmark 2, posterior tip of the headshield. Landmarks 3 and 4, left and right most distal points of the cornual processes, respectively. Inner cornual processes were considered in galeaspids lacking cornual processes. Landmarks 5 and 6, most medial points of the eye orbits (ob.). Landmarks 7–42, type III landmarks situated between Landmarks 1 and 3 and between Landmarks 1 and 4. Landmarks 43–88, type III landmarks situated between Landmarks 2 and 3 and between Landmarks 2 and 4. (c) Diagram of the computational domains used in CFD simulations for pelagic (upper) and benthic (lower) scenarios where models were placed at different angles of attack (bottom left) and different distances above the lower surface of the domain (bottom right). All measurements in mm. Modified from Ferrón *et al.* [14]: fig. 1D.

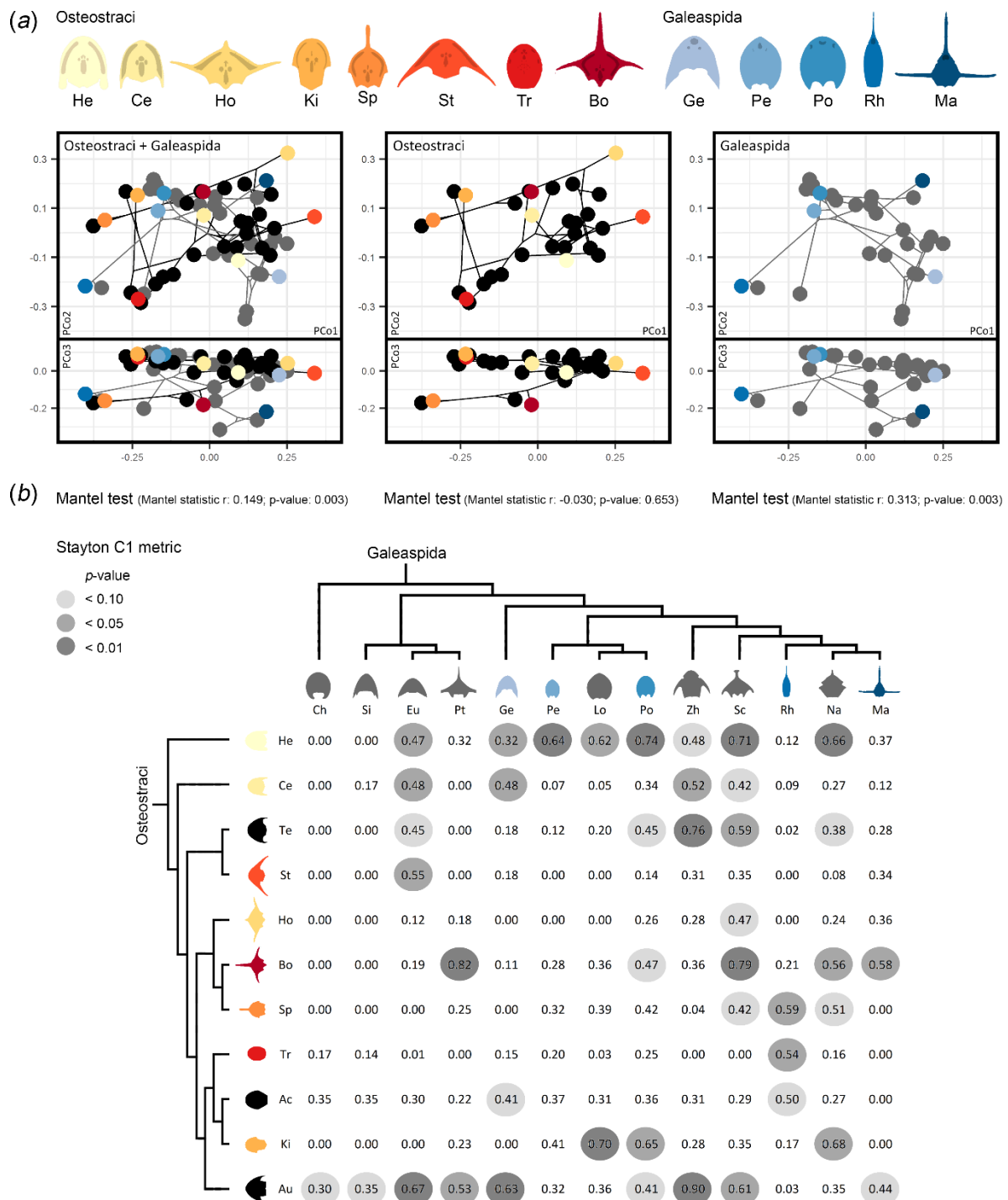


**Figure 2.** Geometric morphometrics and convergence analysis results. (a) Phylomorphospace summarizing the morphological disparity of osteostracan and galeaspid headshields. Ordination of each group is also shown in separate plots to facilitate comparison, but results correspond to a single analysis considering representatives of both groups together. The proportion of variance explained by PCo1–3 is 43.82%, 32.11% and 11.87%, respectively. (b) Mantel test results for each of the datasets (upper) and Stayton C1 metric for several pairs of osteostracans vs galeaspids (lower), indicating different degrees of statistical significance in distinct grey tones. Phylogenetic trees based on Zhu *et al.* [11], Gai *et al.* [13,28], Sansom [10], and Sansom *et al.* [29]. Taxa included in CFD analyses are shown in colour, whereas the rest

of osteostracans and galeaspids are in black and grey, respectively. Osteostraci: non-cornuates (*Hemicyclaspis*, He), Cephalaspida (*Cephalaspis*, Ce), Zenaspidida (*Tegaspis*, Te; *Stensiopelta*, St), Benneviaspidida (*Hoelaspis*, Ho: *Boreaspis*, Bo; *Spatulaspis*, Sp), Kiaeraspidida (*Acrotomaspis*, Ac; *Kiaeraspis*, Ki), and Thyestiida (*Auchenaspis*, Au; *Tremataspis*, Tr). Galeaspida: Xiushuiaspididae (*Changxingaspis*, Ch), Sinogaleaspidae (*Sinogaleaspis*, Si), Eugaleaspidae (*Eugaleaspis*, Eu; *Pterogonaspis*, Pt), Geraspididae (*Geraspis*, Ge), Pentathyraspidae (*Pentathyraspis*, Pe), Duyunolepidae (*Lopadaspis*, Lo), Polybranchiaspidae (*Polybranchiaspis*, Po), Zhaotongaspididae (*Zhaotongaspis*, Zh), Sanchaspidae (*Sanchaspis*, Sc), Gantarostrataspidae (*Rhegmaspis*, Rh), and Huananaspidae (*Nanpanaspis*, Na; *Macrothyaspis*, Ma).

597

598

599

600

601

602

603

604

605

606

607

608

609

610

611

612

613

614

615

616

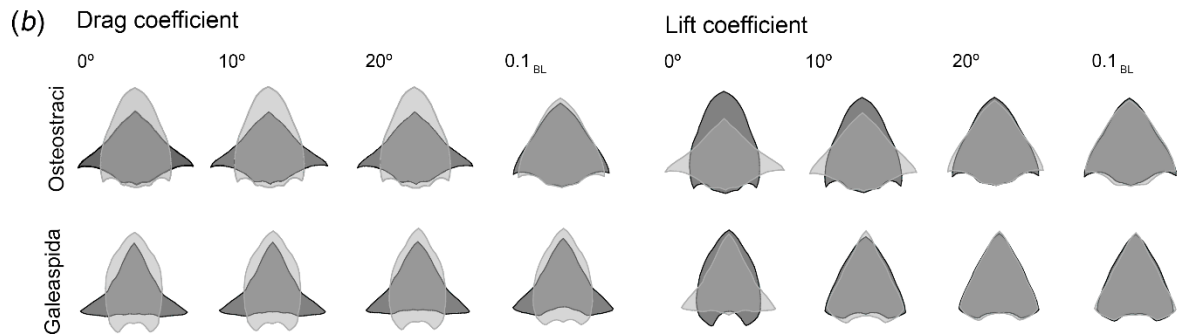
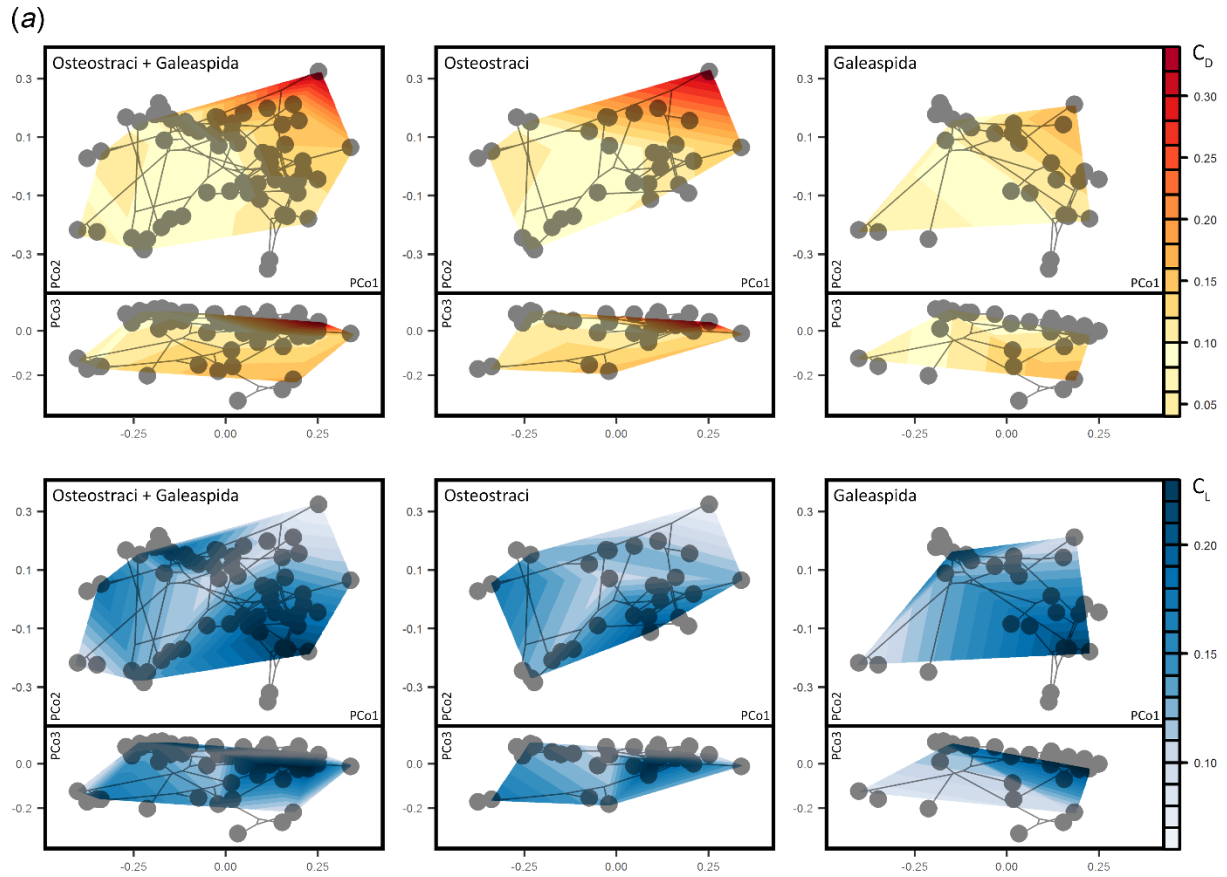


**Figure 3.** Morphological and biomechanical correlates. (a) Drag ( $C_D$ ) and lift ( $C_L$ ) coefficient heat maps plotted over the phylomorphospaces of the whole dataset, osteostracans and galeaspids. Force values correspond to pelagic scenarios considering an angle of attack of  $10^\circ$  with an inlet velocity of  $0.3 \text{ m s}^{-1}$ . (b) Correlations between headshield morphology and hydrodynamic force coefficients ( $C_D$  and  $C_L$ ) calculated under different experimental conditions (i.e., pelagic scenario at angles of attack of  $0^\circ$ – $20^\circ$  and benthic scenario at  $0.1$  body lengths (BL) above the substrate, with an inlet velocity of  $0.3 \text{ m s}^{-1}$ ). Pairs of overlapping outlines (landmark wireframe configurations) represent the headshield morphologies that generate the highest and lowest force coefficients (in darker and lighter grey, respectively) in each scenario. Correlation results of Osteostraci:  $C_D$  ( $0^\circ$ ): % predicted = 46.53,  $p$ -value = 0.0005;  $C_D$  ( $10^\circ$ ): % predicted = 43.36,  $p$ -value = 0.0006;  $C_D$  ( $20^\circ$ ): % predicted = 40.58,  $p$ -value = 0.0014;  $C_D$  ( $0.1_{BL}$ ): % predicted = 35.84,  $p$ -value = 0.0056;  $C_L$  ( $0^\circ$ ): % predicted = 52.69,  $p$ -value = 0.0001;  $C_L$  ( $10^\circ$ ): % predicted = 25.64,  $p$ -value = 0.0317;  $C_L$  ( $20^\circ$ ): % predicted = 4.17,

$p$ -value = 0.5488;  $C_L$  (0.1<sub>BL</sub>): % predicted = 5.39,  $p$ -value = 0.4808. Correlation results of Galeaspida:  $C_D$  (0°): % predicted = 59.09,  $p$ -value = 0.0038;  $C_D$  (10°): % predicted = 57.15,  $p$ -value = 0.0053;  $C_D$  (20°): % predicted = 63.35,  $p$ -value = 0.0011;  $C_D$  (0.1<sub>BL</sub>): % predicted = 38.59,  $p$ -value = 0.0346;  $C_L$  (0°): % predicted = 29.22,  $p$ -value = 0.1064;  $C_L$  (10°): % predicted = 10.87,  $p$ -value = 0.5109;  $C_L$  (20°): % predicted = 11.61,  $p$ -value = 0.4875;  $C_L$  (0.1<sub>BL</sub>): % predicted = 10.92,  $p$ -value = 0.5593.

637

638

639

640

641

642

643

644

645

646

647

648

649

650

651

652

653

654

655

656

657

658

659

660

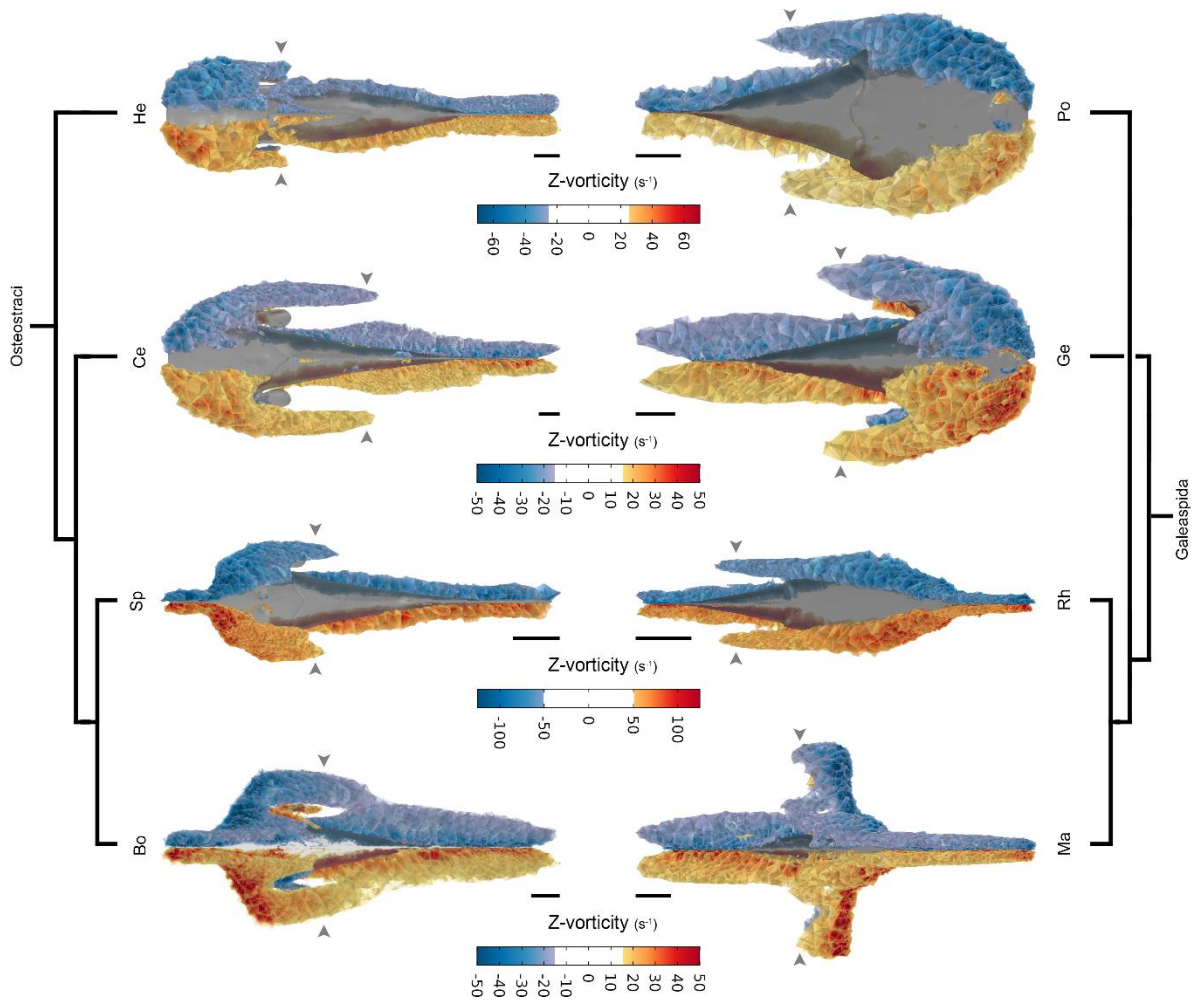


**Figure 4.** Vorticity patterns over osteostracan and galeaspid models under pelagic scenarios considering an angle of attack of 20°. Arrows indicate the position of tip vortices. Species are associated by homoplastic pairs with the highest Stayton C1 values for comparison. Bo, *Boreaspis*; Ce, *Cephalaspis*; Ge, *Geraspis*; He, *Hemicyclaspis*; Ma, *Macrothyraspis*; Po, *Polybranchiaspis*; Rh, *Rhegmaspis*; Sp, *Spatulaspis*. Phylogenetic trees based on Zhu *et al.* [11], Gai *et al.* [13,28], Sansom [10], and Sansom *et al.* [29]. Scale bar 1 cm.